

# Fabrication, Characterization and Dielectric Studies of NBR/Hydroxyapatite Nanocomposites

A. Nihmath<sup>1</sup> · M. T. Ramesan<sup>1</sup>

Received: 25 November 2016 / Accepted: 20 December 2016 / Published online: 7 January 2017  
© Springer Science+Business Media New York 2017

**Abstract** Nitrile rubber (NBR) based nanocomposite consists of different concentrations of hydroxyapatite nanoparticles (HA) were prepared and characterized by FTIR, UV and X-ray diffraction studies. The surface morphology of the nanocomposites were analyzed using SEM and optical microscopy. The glass transition temperature and thermal stability of NBR and its nanocomposites were done by DSC and TGA respectively. The electrical properties such as AC conductivity, dielectric constant and dielectric loss tangent were investigated in the frequency range of  $10^2$ – $10^6$  Hz at room temperature. The FTIR spectra confirmed the interfacial interaction between NBR and the HA nanoparticles. The shift in the UV peak with broadness of composite indicates the formation of nanoparticles within the macromolecular chain of NBR. XRD pattern ascertained the ordered arrangement of nanoparticles with a decrease in the amorphous nature of parent polymer. Both the glass transition temperature and the thermal stability of the nanocomposites were higher than pure NBR and the glass transition temperature improved with the increase in concentration of nanoparticles in NBR composite indicating the strong interfacial adhesion between the polymer and nanoparticles. From DSC studies, thermodynamic parameters such as enthalpy and entropy change of the composites were also evaluated. AC conductivity of the nanocomposite was much greater than NBR and the magnitude of conductivity enhanced with the addition of nanoparticles. The observed enhancement in dielectric constant and dielectric loss tangent of composite with the increase in

concentration of nanoparticle was attributed to the increase in number of interfacial interaction between the polymer and the nanoparticles.

**Keywords** NBR · Hydroxyapatite nanoparticles · Crystallinity · Thermal behavior · Dielectric properties

## 1 Introduction

Polymer based composites with metal particles have extensively attracted by researchers because of their wide applications in electromechanical systems [1–3]. Many scientists have investigated the synthesis and applications of polymer–metal composites and the overall response of the composite depends on the interfacial behaviour and phase morphology of the components [4–6]. Recently, the polymer nanocomposites have been the subject of extensive studies over conventional microcomposites due to exceptionally large interfacial area per unit volume of dispersed phase. This high aspect ratio helps to increase the interaction with the matrix phase which enhances the mechanical, electrical, thermal and optical properties of nanocomposites [7–11].

At present, metal electrodes used to deliver electric current to repair bone damages by the application of electrical stimulation which has many disadvantages such as risk of complication of surgery, limited extent to which electric stimulus could be delivered etc. To overcome these difficulties electrically conducting nanocomposite materials were introduced for biomedical applications [12]. Moreover, polymer with ceramic filler nanocomposites have enormous applications in electrical and electronic devices because of the low temperature processing of polymers and the high dielectric constant of ceramics, used in integrated

✉ M. T. Ramesan  
mtramesan@uoc.ac.in

<sup>1</sup> Department of Chemistry, University of Calicut, Calicut University P.O., Calicut, Kerala 673 635, India

decoupling capacitors, angular acceleration accelerometers, acoustic emission sensors and in electronic packaging.

Hydroxyapatite ( $\text{Ca}_{10}(\text{PO}_4)_6(\text{OH})_2$ ; HA), a nano sized bioceramic crystal having excellent biodegradability, biocompatibility and osteoconductive properties [13], is the major component of natural bone [14]. It has versatile and diverse biomedical applications in tissue engineering, regenerative medicine, gene therapy, controlled drug delivery system etc. [15]. However HA is brittle, can be crushed easily, high temperature processability and is unfit for direct implant applications [16]. Therefore applications of a number of natural and synthetic polymers have been reported as a scaffold for HA in biomedical applications. Chua et al. reported the development of PVA/HA biocomposite as a tissue scaffold for craniofacial and joint defects [17].

The diversity and novelty in performance characteristics of rubber based composite materials have attracted significant interest over the last several years. Acrylonitrile–butadiene copolymer is a synthetic polar rubber, well known for its excellent oil and heat resistance [18]. The moderate cost, processability, better resistance to acids; aliphatic hydrocarbons etc. made it an ideal material for industrial applications. It is commonly used in petroleum and automobile industry to make fuel hoses, gaskets, rollers etc. It is used as sealant in rubber industry especially for lip seal of ball-bearings [19]. However, NBR has poor green strength, flexibility, flame retardancy and electrical conductivity properties. Recently, many researchers are focused on the fabrication of NBR based nanocomposites not only to enhance the mechanical properties of NBR but also for making use of its oil and solvent resistance. Thomas et al. studied the impact of filler geometry and surface chemistry on the degree of reinforcement and thermal stability of nitrile rubber nanocomposites and their studies revealed that the NBR nanosilicate composites showed great impact on the mechanical and thermal properties of the NBR as compared to titanium dioxide and calcium phosphate fillers [20]. Self-extinguishing elastomeric nanomaterials can be prepared by the incorporation of hallosite nanotube and a halogen-free flame-retardant compound into the NBR matrix was reported by Rybinski et al. [21].

In this work, a simple and direct solution casting method has been applied for the preparation of NBR/hydroxyapatite nanocomposite using different concentration of HA nanoparticles. The structural and morphological studies of the composites were examined by XRD and optical microscopy and SEM. The interaction between the acrylonitrile unit of polymer and hydroxyl groups of HA nanoparticles were studied by FTIR and UV spectroscopy. The effect of concentration of nanoparticles on the thermal stability of NBR and the glass transition temperature of the polymer matrix was evaluated by thermogravimetry and differential

scanning calorimetry analysis. Additionally, the electrical properties such as AC conductivity, dielectric constant and dielectric loss tangent of the composites were studied by an impedance analyzer at different frequencies.

## 2 Experimental

### 2.1 Materials and Methods

NBR was supplied by Synthetics and Chemicals Ltd, U.P., India and has an acrylonitrile content of 34%. The other chemicals used, calcium chloride ( $\text{CaCl}_2$ ), ammonium hydrogen phosphate [ $(\text{NH}_4)_2\text{HPO}_4$ ] and ammonium hydroxide ( $\text{NH}_4\text{OH}$ ) were of analytical grade. The capping agent, cetyl trimethyl ammonium bromide (CTAB) was purchased from Himedia chemicals.

#### 2.1.1 Synthesis of Hydroxyapatite Nanoparticles

Hydroxyapatite nanoparticles were prepared by the chemical co-precipitation method as reported previously [22]. A suitable amount of  $\text{CaCl}_2$  and  $(\text{NH}_4)_2\text{HPO}_4$  were prepared in an aqueous solution and these solutions were pre-heated and mixed under vigorous stirring.  $\text{NH}_4\text{OH}$  was added to the reaction mixture immediately after mixing until the pH reached to 10. After stirring for 24 h the precipitate was filtered, washed with water, dried and the HA powder was then sintered at  $600^\circ\text{C}$  for 6h.

#### 2.1.2 Preparation of NBR/Hydroxyapatite Nanocomposite

The NBR/HA nanocomposites were prepared by direct solution casting method. NBR, 100 phr (parts per hundred rubbers) was added to toluene with stirring the solution at room temperature to complete the dissolution. Various amount of HA nanoparticles (3, 5, 7, 10, 15 and 20 phr) were mixed with CTAB in toluene solution and ultrasonicated for 15 min. The NBR homogenous solution was then mixed with various content of HA nanoparticles (3, 5, 7, 10, 15 and 20 phr filler particles in toluene with CTAB) and ultrasonicated again for 20 min and allowed to stir it for 2h. For comparison, a blank compound was also prepared by mixing NBR with toluene. These solutions were then coagulated with ethanol and dried in oven.

#### 2.1.3 Characterization

The IR spectra of the composites were recorded on a JASCO (model 4100) Fourier transform infrared spectrophotometer in the region  $400\text{--}4000\text{ cm}^{-1}$ . The UV spectra of samples were obtained using a Hitachi U-300 spectrophotometer. X-ray diffraction pattern of the sample was

recorded on Rigaku miniflex 600 X-ray diffractometer using CuK $\alpha$  radiation ( $\lambda=1.5406 \text{ \AA}$ ). The diffractogram was recorded in terms of  $2\theta$  in the range  $10\text{--}80^\circ$ . The surface morphology of the rubber was investigated by using Field Emission Scanning Electron Microscopy (FESCA)-Hitachi, SU 6600 (FESEM) after sputter coating of the fracture surface with gold at  $0^\circ$  tilt angle. The optical images of the composites were carried out by trinocular microscope Model Axio Lab.A1 attached AxioCam ERc5s Carl Zeiss Microimaging GmbH analyzer. Thermal decomposition behavior of the nanocomposites was investigated by a Perkin Elmer thermo gravimetric analyzer at a heating rate of  $10^\circ\text{C}/\text{min}$  in a dry nitrogen atmosphere. DSC analysis was carried out by Mettler Toledo DSC 22e at a heating rate of  $5^\circ\text{C}/\text{min}$  (atmosphere  $\text{N}_2$ ; flow  $40 \text{ ml}/\text{min}$ ). AC resistivity of the samples was measured by Hewlett–Packard LCR meter, fully automatic system in a frequency range  $100\text{--}10^6 \text{ Hz}$  at room temperature. Dielectric constant or relative permittivity was calculated using the formula

$$\epsilon r = \frac{C \cdot d}{\epsilon_0 \cdot A}$$

where  $d$  be the thickness of the sample,  $C$  the capacitance,  $A$  the area of cross section of the sample and  $\epsilon_0$  be the permittivity of free space and  $\epsilon_r$ , the relative permittivity of the material is a dimensionless quantity. From these dielectric measurements dielectric loss tangent ( $\tan \delta$ ) was also determined.

### 3 Results and Discussion

#### 3.1 FTIR Analysis

The FTIR spectra of HA, NBR and nanocomposites embedded with different concentrations of HA nanoparticles are shown in Fig. 1, and the different assignments obtained from the infrared bands of polymeric materials are summarized in Table 1. NBR shows the characteristic absorption peak at  $2239 \text{ cm}^{-1}$  which is characteristic of CN stretching vibration. The peaks at  $975$  and  $695 \text{ cm}^{-1}$  are assigned to CH wagging of *trans* and *cis*  $-\text{CH}=\text{CH}$  unit of butadiene segment respectively. The peaks at  $1444$  and  $1301 \text{ cm}^{-1}$  represent the absorptions of  $\delta(\text{C}-\text{H})$  of  $-\text{CH}_2$  and for  $\gamma(\text{CH}_2)$  of  $-\text{CH}_2$  respectively. The characteristic absorption peak of HA nanoparticle is observed at  $3573 \text{ cm}^{-1}$  is assigned to stretching vibration of OH ions and peak at  $633 \text{ cm}^{-1}$  indicates the O–H deformation mode. The peaks at  $470$ ,  $569$ ,  $604$ ,  $964$  and  $1045 \text{ cm}^{-1}$  are the characteristic of  $\text{PO}_4^{3-}$  entity. The distinguishable peak at  $964 \text{ cm}^{-1}$  is attributed to P–O stretching vibration of  $\text{PO}_4^{3-}$  and the sharp peak at  $633$ ,  $602$  and  $568 \text{ cm}^{-1}$  are corresponding to bending vibration of  $\text{PO}_4^{3-}$  unit

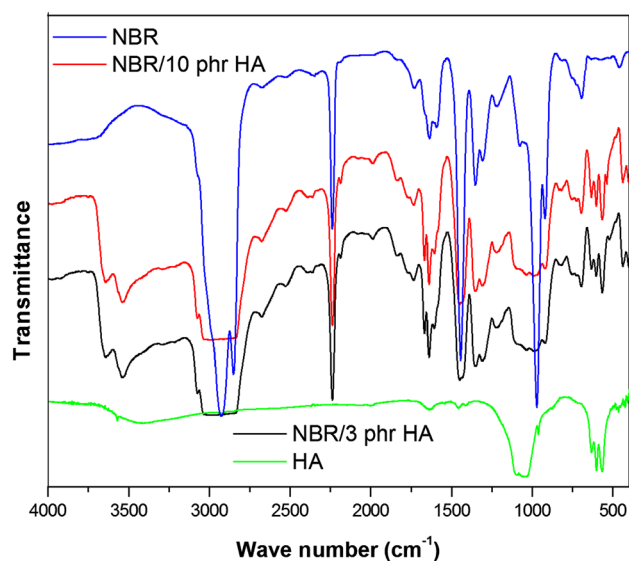


**Fig. 1** FTIR spectra of HA, NBR and its nanocomposite with different content of HA nanoparticles

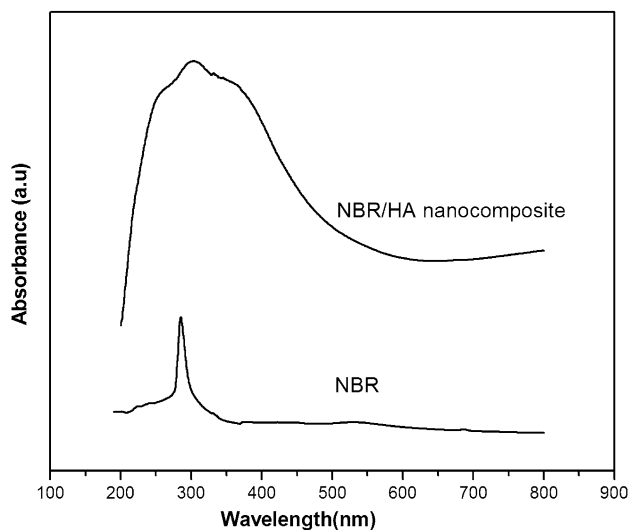
of HA [23]. However, in FTIR spectrum of NBR/HA nanocomposites, the stretching and deformation peak of hydroxyl group of nanoparticle is appeared at  $3636$  and  $695 \text{ cm}^{-1}$ . In addition, the characteristic absorption peaks of phosphate group ( $1045$ ,  $964 \text{ cm}^{-1}$ ) in the nanocomposites slightly shifted to a lower wavenumber at  $985$  and  $918 \text{ cm}^{-1}$ . It is also clear from the figure that the absorption frequencies of composites below  $1000 \text{ cm}^{-1}$  are strongly influenced by the presence of nanoparticles. The shifting of absorption frequencies and appearance of new peaks in the composites (the presence of HA particles at  $567$  and  $601 \text{ cm}^{-1}$  for 3 phr composite while  $561$  and  $613 \text{ cm}^{-1}$  for 10 phr composite) indicates the intermolecular interaction between the polar groups of NBR with the polar group of HA nanoparticles.

#### 3.2 UV–VIS Spectroscopy

The UV–Vis spectra of NBR and NBR/15 phr HA nanocomposite is shown in Fig. 2. NBR shows a sharp low intense absorption peak at  $285 \text{ nm}$  corresponds to  $n-\pi^*$  transition of  $-\text{CN}$  group in the NBR. In the case of nanocomposite the characteristic peak assigned to  $n-\pi^*$  transition is shifted to a higher wavelength region with an intense broad band at  $302 \text{ nm}$ . The increase in intensity and broadness of UV absorption peak in the nanocomposite compared to the UV absorption in neat NBR confirms the increase in crystalline phase of the rubber. The orientation of nanoparticles in the polymer is mainly due to the intermolecular interaction between the polar group of rubber and hydroxyapatite nanoparticles.

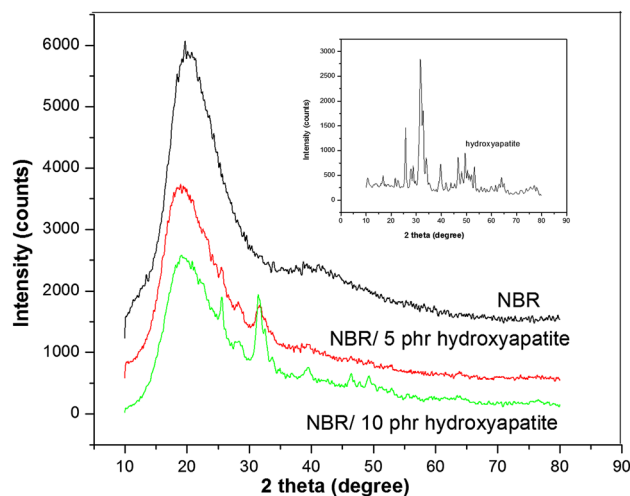
**Table 1** Assignments of the infrared bands of NBR, HA and NBR/HA nanocomposite

Materials	Wave number (cm <sup>-1</sup> )	Assignments
NBR	2932 and 2848	$\nu(\text{CH}_3-, -\text{CH}_2-, >\text{CH}-)$ asymmetric stretching vibration
	2239	$\nu(\text{CN}-)$ stretching vibration
	1647	$\nu(-\text{CH}=\text{CH}-)$ symmetric stretching vibration
	1444	$\delta(-\text{CH}_2-)$ bending vibration
	1301	$\gamma(\text{CH}_2)$ rocking vibration
	975	<i>Trans</i> $\delta(-\text{CH}=\text{CH}-)$ wagging motion vibration
	695	$\delta(\text{CH}_2=\text{CH}-)$ bending vibration
	HA	964, 470, 1045 and 604
633, 602 and 568		( $\nu_4$ ) bending vibration of $\text{PO}_4^{3-}$ unit
964		( $\nu_1$ ) P–O stretching vibration of $\text{PO}_4^{3-}$
3573		( $\nu$ ) stretching vibration of OH
NBR/HA/3phr	3636	( $\nu$ ) stretching peak of hydroxyl group
	695	( $\delta$ ) deformation peak of hydroxyl group
	981	( $\nu_3$ ) vibration modes of phosphate group
	916	( $\nu_1$ ) vibration modes of phosphate group
NBR/HA/10phr	567 and 601	( $\nu_1, \nu_2$ ) bending vibration of phosphate group
	3649	( $\nu$ ) stretching peak of hydroxyl group
	697	( $\delta$ ) deformation peak of hydroxyl group
	981	( $\nu_3$ ) vibration modes of phosphate group
	918 and 613	( $\nu_1, \nu_2$ ) bending vibration of phosphate group

**Fig. 2** UV spectra of NBR and NBR/15 phr HA nanocomposite

### 3.3 X-ray Diffraction Analysis (XRD)

Figure 3 shows the X-ray diffraction pattern of synthesized HA nanoparticles, NBR and NBR/HA nanocomposites with different contents of HA nanoparticles. The XRD pattern of pure HA has been matched with the JCPDS data (9-432) of HA. The various diffraction peaks observed are at  $2\theta = 25.7^\circ, 31.6^\circ, 32.7^\circ, 34.1^\circ, 39.7^\circ, 46.6^\circ, 49.5^\circ,$

**Fig. 3** XRD pattern of HA, NBR and different loadings of HA particles incorporated NBR

$53.09^\circ$ , corresponding to the diffraction of 002, 211, 300, 202, 310, 222, 213, 321, 004 crystal planes respectively [24]. The particle size of HA nanoparticle has determined from the width of XRD peak by using Scherrer's formula.

$$D = K\lambda/\beta \cos \theta$$

where  $K$  is the particle shape factor generally taken as 0.89,  $\lambda$  is the wavelength of  $\text{CuK}\alpha$  radiation  $\lambda = 1.54 \text{ \AA}$ ,  $\theta$  is the diffraction angle of the intense peak, and  $\beta$  is the half

height of diffraction angles in radians. When the reflecting peaks at  $2\theta=31.46^\circ$ , is chosen to calculate the average diameter and the particle size of HA is found to be 9.5 nm. The XRD pattern of NBR showed a broad diffraction peak at  $2\theta=19.72^\circ$  corresponds to the amorphous nature of the polymer. The XRD pattern of nanocomposite shows some characteristic diffraction peaks of HA nanoparticles with the broad amorphous diffraction of NBR. Moreover, the characteristic amorphous diffraction peak of NBR in the composite is found to be shifted to a lower  $2\theta$  value (i.e. from  $19.72^\circ$  to  $18.94^\circ$ ) with a decrease in broadness of the amorphous peak. The strong intermolecular interaction between the rubber and HA nanoparticles imparts a regular arrangement of filler particles within the polymer, leading to some extent of crystallinity in the rubber matrix.

## 4 Morphology Studies

### 4.1 Optical Microscopy

The dispersion of nanoparticles into NBR has been characterized by optical microscopy. Figure 4 shows the optical images of different contents of HA nanoparticles with NBR. It is clear from the micrographs that the lower concentration of nanoparticle (7 phr composite) shows almost uniform morphology with good uniformity of nanoparticles and when the concentration of nanoparticles increased to 15 phr, its uniformity changes to an irregular nature due to the agglomeration of nanoparticles inside the macromolecular chain of NBR.

### 4.2 Scanning Electron Microscopy (SEM)

Figure 5 shows the SEM images of NBR with 7 and 15phr of HA nanoparticles. It is already reported that the morphology of polymer nanocomposite depends on compatibility of the polymer and filler particles and also the size of nanoparticles [25]. The SEM micrograph of NBR exhibits

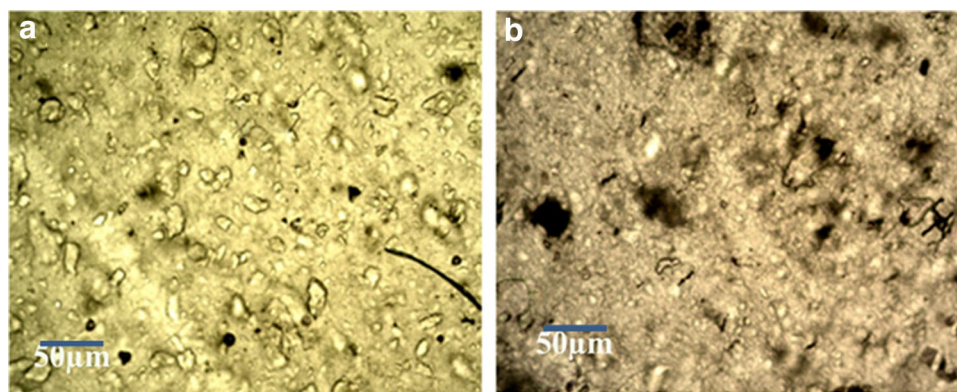
a smooth surface. The morphology of the composite with 7 phr of HA nanoparticles shows a uniform dispersion of particles in NBR matrix. Since the nanoparticles possess large surface area so that they have high affinity to polar macromolecule leading to a uniform orientation of nanoparticles within the NBR chain. As the loading of nanoparticle becomes 15 phr, the composite shows an irregular structure with heterogeneous dispersion of nanoparticles. At higher loadings of fillers, greater stress is developed due to the high external force in the rubber which results in the agglomeration of hydroxyapatite nanoparticles.

## 5 Thermal Behavior

### 5.1 Thermogravimetric Analysis (TGA)

The thermal decomposition behaviour of NBR and NBR with different concentration of HA nanoparticles is given in Fig. 6. It can be observed from the figure that the NBR shows single stage decomposition temperature at  $405^\circ\text{C}$  whereas the NBR nanocomposites with 5 and 15 phr of HA nanoparticles show the thermal degradation at  $415$  and  $413^\circ\text{C}$  respectively. The degradation temperature of nanocomposite is greater than that of NBR which reveals that the nanocomposites exhibit higher thermal stability than that of raw rubber. This is because of the reduced air permeability in to the macromolecular chain and also due to increased crystallinity as a result of the systematic arrangement of macromolecular chain due to the intermolecular interaction between the nanoparticle and the rubber chain. It can be seen from the figure that the char residue obtained at  $600^\circ\text{C}$  for NBR and nanocomposites with 5 and 15 phr HA are 2.4, 13.3 and 17.1% respectively. This indicates that the nanocomposite shows higher percentage of final char residue than pure NBR. The increased char residue of nanocomposites suggests the better flame retardancy of the nanocomposite.

**Fig. 4** Optical micrographs of **a** NBR/7 phr HA and **b** NBR/15 phr HA nanoparticles



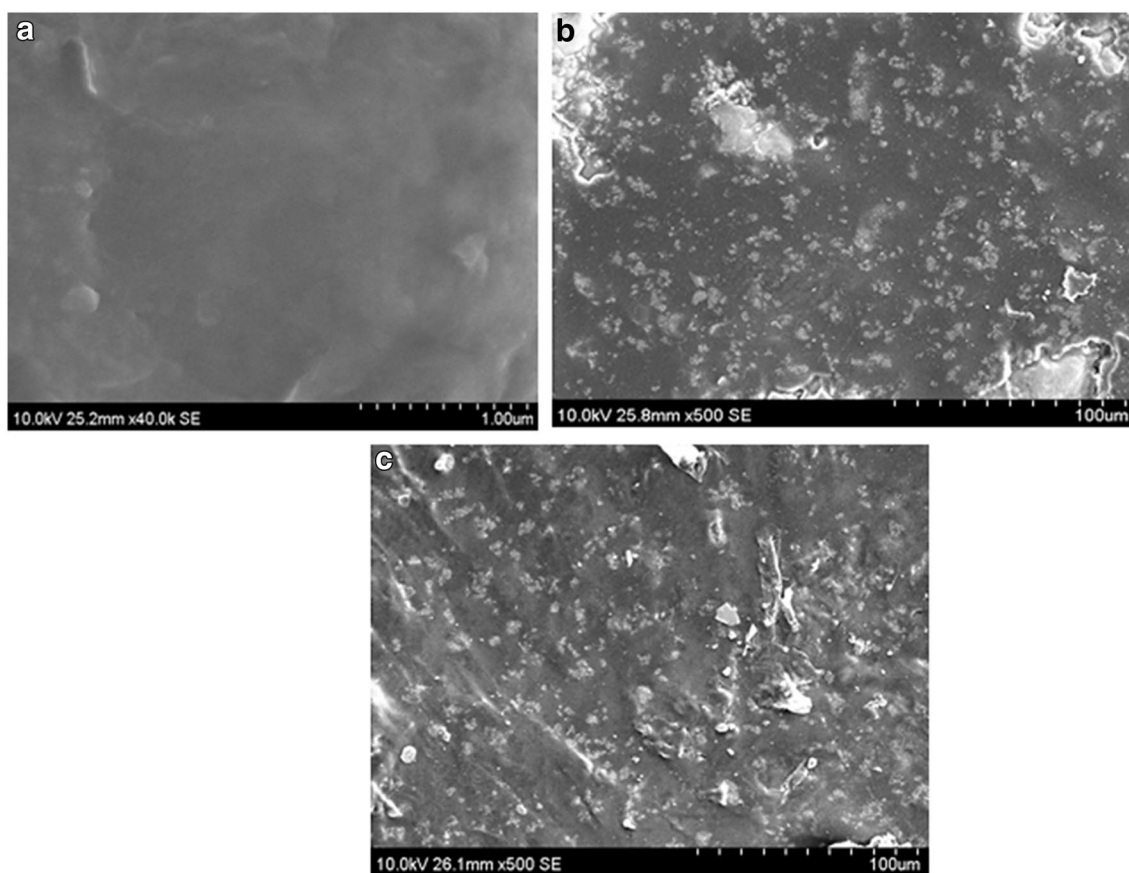


**Fig. 5** SEM images of **a** NBR, **b** NBR with 7 phr and **c** NBR with 15 phr HA nanoparticles

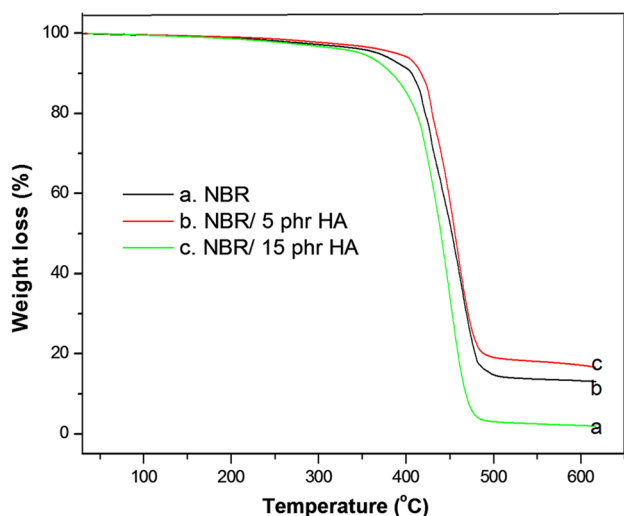


**Fig. 6** Thermal degradation pattern of NBR and NBR with 5 and 15 phr of HA nanoparticles

## 5.2 Differential Scanning Calorimetry (DSC)

The glass transition temperature and the thermodynamic properties of fabricated nanocomposites were studied by

differential scanning calorimetry (DSC). The DSC curve of pure NBR and the composite filled with 7 and 15 phr of HA nanoparticles are presented in Fig. 7. The glass transition temperature ( $T_g$ ) of pure NBR is occurred at  $-35.6^\circ\text{C}$ . The  $T_g$  of all composite filled with nano sized HA particles increases significantly as the volume fraction of filler raises. The  $T_g$  values obtained for 7 and 15 phr of nanoparticles are at  $-32.5^\circ\text{C}$  and  $-30.4^\circ\text{C}$  respectively. Generally, the glass transition temperature of rubber composite depends mainly on the polarity and crystallinity of polymer and the filler particles. The increment in  $T_g$  with respect to filler loading is assigned to the polar–polar interaction between the hydroxyl group of apatite nanoparticles and the nitrile group of NBR creates structural regularity in the rubber and thereby retards the mobility of the rubber chain. It has also been reported that the elastomeric material posses high  $T_g$  have higher crystallinity and the knowledge of  $T_g$  is much important in the manufacturing process of rubber products. Further, the glass transition of amorphous rubber may be due to the change in heat capacity of sample undergoing calorimetric measurement. The heat of fusion ( $\Delta H$ ) and corresponding entropy change ( $\Delta S$ ) at glass phase transition was measured from the DSC

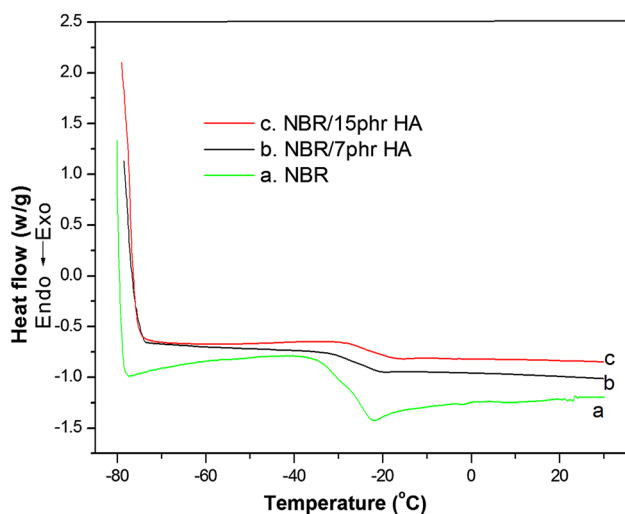


**Fig. 7** DSC thermograms of NBR and NBR with different contents of HA nanoparticles

curve. NBR shows the  $\Delta H$  value of  $227.58 \text{ KJ mol}^{-1}$  and  $\Delta S$  around  $14.29 \text{ JK}^{-1} \text{ mol}^{-1}$ . However the  $\Delta H$  value of nanocomposite with 7 and 15 phr of nanoparticle exhibits respectively at  $83.58$  and  $72.17 \text{ KJ mol}^{-1}$ . Similarly the  $\Delta S$  value obtained for 7 and 15 phr of nanocomposite is  $5.41$  and  $4.73 \text{ JK}^{-1} \text{ mol}^{-1}$  respectively. From these values it can be inferred that as compared to amorphous NBR, the nanocomposite shows lower enthalpy and entropy of transition. Also, the  $\Delta H$  and  $\Delta S$  value decreases with increasing the loading of nanoparticles in the macromolecular chain of NBR. Thus the lower of heat of fusion and disorderness of composite with increased glass transition temperature again confirms the interaction of polymer chain with the nanoparticles [26, 27].

### 5.3 Conductivity Studies

#### 5.3.1 AC Conductivity

Figure 8 shows the variation in AC conductivity with various frequencies of pristine NBR and nanocomposite containing different loadings of HA as double logarithmic plots of  $\sigma_{AC}$  vs. frequency. The conductivity improved with the increase in frequency indicates the electronic conduction in the composite materials is of hopping type. Thus the transportation of charge carriers which are decoupled from the elastomer segmental motion occurs through hopping process. It is well clear from the figure that the conductivity of nanocomposites are much higher than the pure NBR which is due to the uniform dispersion of nanoparticles and thereby the regular arrangement of nanoparticles in the polymer matrix. Moreover, the extensive interfacial zone, the orientation of dipoles associated with the nitrile

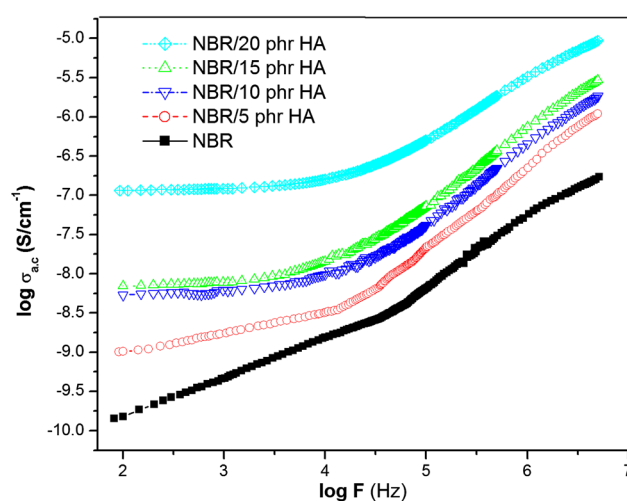


**Fig. 8** AC conductivity of NBR and NBR/HA nanocomposites

group of NBR and the hydroxyl group of hydroxyapatite nanoparticle is responsible for the higher conductivity in the nanocomposite. Also, the conductivity is related to the polarity of the composite material, crystallinity of the sample and the orientation of dipoles in the macromolecular chain of NBR. It is evident from the XRD studies that the crystallinity of the nanocomposite increases with the loadings of nanoparticles. The same results are also found in the literatures [28, 29]. The conductivity of nanocomposites is found to be improved with the concentration of nanoparticles. The compactness of composite materials is increased by the addition of apatite nanoparticles, which improves the links between the grains and therefore coupling through grain boundaries became stronger, that leads to a higher conductivity values.

#### 5.3.2 Dielectric Constant

The dielectric properties are measured to understand the polarization mechanism arising from the alignment of charge carriers under applied field. Figure 9 depicts the variation of dielectric constant with frequency for NBR and NBR containing different concentration of HA nanoparticles. It is clear from the figure that the dielectric constant continuously decreases with increase in frequency and attains a constant value at higher frequencies. The increase in dielectric constant may be due to interfacial polarization which arises from the polar interaction of functional groups present in the surface of polymer and hydroxyl group of nanoparticles [30]. The high dielectric value at lower frequency is due to the dipoles get enough time to align before it changes its direction while as the applied frequency increases there will be insufficient time for dipoles to align before the reversal of field. The dielectric constant

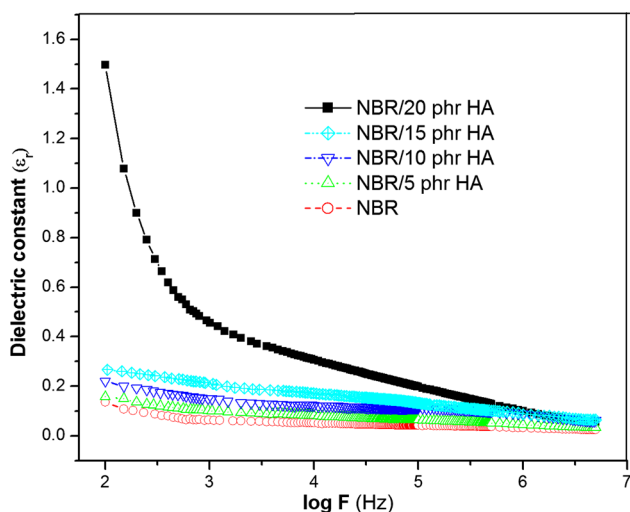


**Fig. 9** Dielectric constant of NBR and its nanocomposite with various contents of HA nanoparticles

continuously increases with increasing the loadings of nanoparticles and an abrupt increase in dielectric constant of composite is noticed when the volume fraction of filler particles reached to 20 phr. This sharp increase is a direct consequence of enhanced interfacial polarization effect between the nanoparticles and rubber [31]. The higher dielectric constant indicates higher capacitance density of the nanocomposites which is proportional to the quantity of charge stored on the surface of composite materials under an applied electric field. In the present study, the quantity of the accumulated charge is high due to the polarization of NBR with the HA nanoparticles at the interface. From this point of view, it can be inferred that the dielectric constant of nanoparticles are much higher than pure NBR and the dielectric constant depends on the loadings of nanoparticle in the rubber matrix [32].

### 5.3.3 Dielectric Loss

The variation of the dielectric loss tangent ( $\tan \delta$ ) of NBR/HA nanocomposites as a function of frequency at room temperature is reproduced in Fig. 10. The relaxation processes arising from the structural reorganization of the material is responsible for the dielectric loss factor. The dielectric loss tangent decreases steeply at lower frequencies and reaches a constant value at higher frequencies ( $10^4$  Hz). This is mainly due to the induced charges gradually loses to follow the reversing field, which leads to a reduction in the electronic oscillation as the frequency is increased [33]. The  $\tan \delta$  values of the composites are significantly higher than pure NBR and the dielectric loss tangent improved with the volume fraction of nanoparticles. The maximum dielectric loss tangent is noted for 20 phr

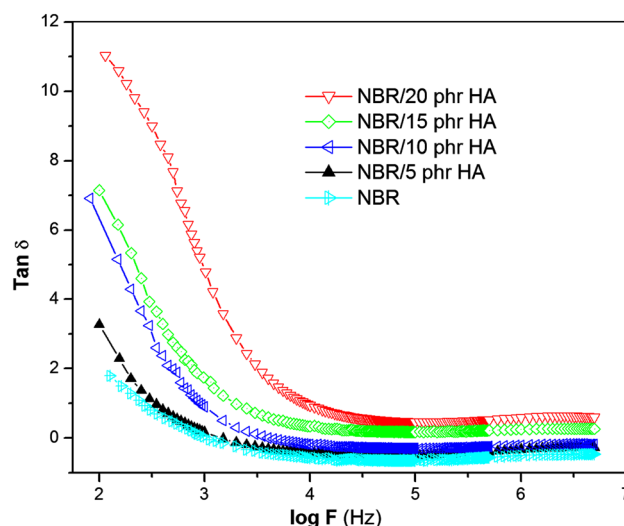


**Fig. 10** Dielectric loss tangent of NBR and NBR/HA nanocomposites

of composite and this is because of the strong intermolecular interaction between the filler surface and the NBR chain which leads to higher crystallinity. Thus the influence of HA on dielectric loss of composite can be ascribed to the increased regularity of polymer chain which is in good agreement with XRD studies.

## 6 Conclusions

NBR nanocomposite with different concentration of hydroxyapatite nanoparticles were prepared by solution casting technique. FT-IR spectra revealed the appearance of new peak and shifting of some absorption frequencies. This was attributed to the strong intermolecular interaction between hydroxyapatite nanoparticles and the acrylonitrile unit of NBR. UV spectrum of the composite showed the shift of absorption maximum with the broadening of UV peak was an indication of the decrease in amorphous nature of composite materials. XRD analysis showed that the HA nanoparticles were coated with NBR segments and the intensity of the XRD peaks increased with the loadings of nanoparticles. The optical micrographs gave the good dispersion of nanoparticle into the rubber matrix. SEM images clearly reflect the uniform dispersion of hydroxyapatite nanoparticles in NBR matrix. An increase in thermal decomposition temperature with the incorporation of apatite nanoparticles in NBR was observed by TGA. DSC results showed that the NBR/HA composites have higher glass transition temperature than pure NBR and the glass transition temperature of all the composites were significantly improved as the volume fraction of filler increases. The nanocomposite showed lower enthalpy and



entropy of transition than pure NBR. The AC conductivity considerably enhanced with the increase in loading of nanoparticles and the conductivity of the all composites were higher than pure NBR. The dielectric constant decreases slowly with increasing frequency and a higher dielectric constant observed for composite with 20 phr of loading. The dielectric loss tangent ( $\tan \delta$ ) of composite was higher than the NBR and the  $\tan \delta$  values increases gradually with a raise of volume fraction of nanoparticles. The high dielectric properties of the composites were arising due to the increased interaction between nanoparticles and the polymer that result in an ordered arrangement of filler inside the macromolecular chain of NBR. The enhanced dielectric and electrical conductivity of composite proposes a potential application in the field of nanotechnology where the flexibility of the product is required and the conductivity range of composite material suggest that it can be used for ESD application also.

**Acknowledgements** The authors wish to thank Prof. P. P. Pradyumnan, Department of Physics, University of Calicut for providing necessary facilities in the department. The authors (Nihmath) also wish to thank University Grants Commission, New Delhi for their financial assistance.

## References

- R. Rajendran, L.K. Shrestha, R.M. Kumar, R. Jayavel, J.P. Hill, K. Ariga, *J. Inorg. Organomet. Polym.* **25**, 267 (2015)
- E. Bet-moushoul, Y. Mansourpanah, K. Farhadi, M. Tabatabaei, *Chem. Eng. J.* **283**, 29 (2016)
- N. Tanaka, A. Okazawa, A. Sugahara, N. Kojima, *Bull. Chem. Soc. Jpn.* **88**, 1150 (2015)
- P. Jayakrishnan, M.T. Ramesan, *Mater. Chem. Phys.* **186**, 513 (2017)
- H.M. Shiri, A. Ehsani, *Bull. Chem. Soc. Jpn.* **89**, 1201 (2016)
- V.K. Thakur, R.K. Gupta, *Chem. Rev.* **116**, 4260 (2016)
- M. Balachandran, S.S. Bhagawan, *J. Polym. Res.* **19**, 9809 (2012).
- M.T. Ramesan, P. Jayakrishnan, *J. Inorg. Organomet. Polym.* (2016). DOI:10.1007/s10904-016-0456-x
- Z. Han, J. Zhang, X. Yang, H. Zhu, W. Cao, *J. Inorg. Organomet. Polym.* **20**, 32 (2010)
- K. Jayakrishnan, A. Joseph, B. Jayakrishnan, M.T. Ramesan, K. Chandrasekharan, N. K.S. Narendran, *Opt. Mater.* **54**, 252 (2016)
- R.P. Sing, A. Tiwari, C. Pandey, *J. Inorg. Organomet. Polym.* **21**, 788 (2011)
- G. Kaur, R. Adhikari, P. Cass, M. Brown, T. Gunathilake, *RSC Adv.* **5**, 37553 (2015).
- F. Chen, Z.C. Wang, C.J. Lin, *Mater. Lett.* **57**, 858 (2002)
- M. Swetha, K. Sahithi, A. Moorthi, N. Srinivasan, K. Ramasamy, N. Selvamurugan, *Int. J. Bio. Macromol.* **47**, 1 (2010)
- H. Tian, Z. Tang, X. Zhuang, X. Chen, X. Jing, *Progr. Polym. Sci.* **37**, 237 (2012)
- C. Kealley, M. Elcombe, A.V. Riessen, B.B. Nissan, *Physica B.* **385–386**, 496 (2006)
- C.K. Chua, K.F. Leong, K.H. Tan, F.E. Wiria, C.M. Cheah, *J. Mater. Sci.* **15**, 1113 (2004)
- T. Yasin, S. Ahmed, F. Yoshii, K. Makuuchi, *React. Funct. Polym.* **57**, 113 (2003)
- J. M. Degrange, M. Thomine, P. Kapsa, J. M. Pelletier, L. Chazeau, G. Vigier, G. Dudragne, L. Guerbe, *Wear* **259**, 684 (2005).
- P. C. Thomas, S. P. Thomas, G. George, S. Thomas, J. Kuruvilla, *J. Polym. Res.* **18**, 2367 (2011).
- P. Rybinski, G. Janowska, *Thermochim. Acta.* **549**, 6 (2012).
- X.X. Pang, X. Bao, *J. Eurp. Ceram. Soc.* **23**, 1697 (2003)
- E. Nejadi, V. Firouzidor, M.B. Eslamnejad, F. Bagheri, *Mater. Sci. Eng. C.* **29**, 942 (2009)
- P.M.S.L. Shanthi, R.V. Mangalaraja, A.P. Uthirakumar, S. Velmathi, T. Balasubramanian, M. Ashok, *J. Colloid Interface Sci.* **350**, 39 (2010)
- P. Jayakrishnan, M.T. Ramesan, *J. Inorg. Organomet. Polym.* (2016). DOI:10.1007/s10904-016-0474-8
- M.T. Ramesan, *J. Appl. Polym. Sci.* **131**, 3681 (2014)
- M.T. Ramesan, T.K.M. Kumar, R. Alex, B. Kuriakose, *J. Mater. Sci.* **37**, 109 (2002)
- P. Jayakrishnan, P.P. Pradyumnan, M.T. Ramesan, *Chemist* **89**, 27 (2016).
- M.T. Ramesan, V.K. Athira, P. Jayakrishnan, C. Gopinathan, *J. Appl. Polym. Sci.* **133**, 5827 (2016)
- R.M. Mors, M.N. Ismaiel, A.A. Yehia, *Int. J. Mater. Method Tech.* **1**, 22 (2013)
- M.T. Ramesan, K. Surya, *J. Appl. Polym. Sci.* **133**, 43496 (2016)
- D. Yu, J. Wu, L. Zhou, D. Xie, S. Wu, *Comp. Sci. Technol.* **60**, 499 (2000).
- A. Qureshi, A. Mergen, M.S. Eroğlu, N.L. Singh, A. Gulluoglu, *J. Macromol. Sci.* **45**, 462 (2008).